Journal of Environmental Chemical Engineering 13 (2025) 118575

Contents lists available at ScienceDirect

Journal of Environmental Chemical Engineering

journal homepage: www.elsevier.com/locate/jece

Investigation on Ni/CeO_2 catalyst derived from Ce-MOFs for CO_2 hydrogenation to methane

Meirong Dong [a,b,c,*], Jinke Wu [a,b,c], Junshu Yang [a], Hongchuan Liu [a,b,c], Xi Chen [a], Zehua Huang [a,b,c], Jidong Lu [a,b,c]

[a] School of Electric Power Engineering, South China University of Technology, Guangzhou, Guangdong 510640, PR China
[b] Guangdong Province Key Laboratory of Efficient and Clean Energy Utilization, Guangzhou 510641, China
[c] Guangdong Province Engineering Research Center of High Efficient and Low Pollution Energy Conversion, Guangzhou, Guangdong 510640, PR China

ARTICLE INFO

Keywords:
CO_2 methanation
Nickel-based catalyst
Metal-organic frameworks
Oxygen vacancy

ABSTRACT

The continued reliance on traditional fossil fuels and the consequent accumulation of greenhouse gases has made CO_2 conversion and utilization a critical issue for sustainable global development. Hydrogenating CO_2 to methane offers a promising method by harnessing renewable energy sources. In this work, we systematically studied the catalytic performance of the Ce-MOFs-derived Ni/CeO_2 catalysts (10 wt% Ni loading) in CO_2 hydrogenation to methane. The metal-organic frameworks (MOFs) exhibit a distinctive pore structure that enables the effective dispersion of active Ni species on the CeO_2 surface. This feature prevents Ni agglomeration and sintering at elevated temperatures, thereby enhancing catalytic activity. Characterization (XRD, TEM, N_2 adsorption–desorption, XPS, Raman and CO_2-TPD) results show that the morphology of the support significantly impacts catalytic performance in CO_2 reduction. The rod-like Ni/CeO_2-BTC catalyst contains more oxygen vacancies, which improves its ability to adsorb and activate CO_2 on the surface of Ni-CeO_2. Consequently, Ni/CeO_2-BTC demonstrates the highest CO_2 conversion, reaching 61.9 %, and methane selectivity, reaching 85.8 % at 375 ℃ and atmospheric pressure. Density functional theory (DFT) calculation results also confirm that, in the presence of oxygen vacancies, CO_2 is more easily adsorbed and activated at the interface of Ni-O-Ce. The research revealed the intrinsic relationship between reactivity and microscopic physical-chemical properties, as well as the activation mechanism of CO_2, which is crucial to develop Ni/CeO_2 catalysts with various morphologies for CO_2 methanation.

1. Introduction

Nowadays, the global consumption of non-renewable fossil fuels, including coal and oil, surges to meet the growing demand for energy [1,2]. Meanwhile, the massive burning of these fuels generates excessive carbon emissions, driving carbon dioxide (CO_2) accumulation in the atmosphere, which in turn exacerbates global warming and the greenhouse effect. Carbon capture, utilization, and storage (CCUS) technologies have emerged as critical strategies in the effort to cope with these challenges. The utilization of undesirable CO_2 offers an efficient pathway for yielding valuable chemical compounds such as fuels and chemicals [3,4]. Among various optional routes, the utilization of "green" hydrogen produced by renewable energy-driven for the CO_2 reduction to methane (Sabatier reaction), as shown in Eq. (1), has garnered extensive research attention for its benefits: (1) A proved alternative to CO_2 recycling; (2) Methane (CH_4) is an essential basic raw material for the synthesis of other chemicals [5,6]. This reaction also is regarded as an effective way to achieve safe hydrogen energy storage and transportation through chemical transformation [7].

$$CO_2(g) + 4H_2(g) \rightarrow CH_4(g) + 2H_2O(g)\ \Delta_r H_m^{298K} = -164.9 kJ{\cdot}mol^{-1} \quad (1)$$

Sabatier reaction is well-known to be exothermic, thus thermodynamically favors at lower-level reaction temperature [8]. However, since the thermodynamic stability of CO_2 molecules, extra energy is required to activate the C═O duplex or an effective catalyst to cut down the activation energy. Several studies have already been conducted on the development of catalysts based on active components from precious metals or non-precious metals, and their catalytic behavior in CO_2 hydrogenation under diverse reaction conditions has been explored [9]. Due to the relatively low cost, great availability, and excellent catalytic

* Corresponding author at: School of Electric Power Engineering, South China University of Technology, Guangzhou, Guangdong 510640, PR China.
E-mail address: epdongmr@scut.edu.cn (M. Dong).

https://doi.org/10.1016/j.jece.2025.118575
Received 22 May 2025; Received in revised form 25 July 2025; Accepted 8 August 2025
Available online 9 August 2025

performance, diverse Nickel-based catalysts, including Ni/Al_2O_3[10], Ni/SiO_2[11], Ni/ZrO_2[12], have been performed for CO_2 hydrogenation to CH_4. Cerium (Ce) is the most abundant element among rare earth elements, and its oxide CeO_2 is widely used as a support in various catalytic reactions as its abundant oxygen vacancies and unique redox properties [13,14]. Moreover, the valence switch between Ce^{3+} and Ce^{4+} promotes the formation of VOs, which could enable relatively more CO_2 to adsorb on the catalyst surface thereby facilitating CO_2 activation. Zhou et al. [15] prepared Ni/CeO_2 catalyst by conventional impregnation method and achieved approximately 91.1 % CO_2 conversion, which was attributed to the redox cycle formed on the surface of Ni/CeO_2 catalyst. Unfortunately, for the CO_2 methanation, the traditional metal/carrier Ni-based catalysts are prone to loss the activity at high temperature owing to agglomeration, sintering and carbon deposition [16, 17]. A proposed strategy to this issue is to develop metal-based catalysts with high dispersion, which could achieve efficient and stable CO_2 reduction.

Recently, diverse rational design strategies have been employed to boost catalytic performance, encompassing metal-doped, optimizing metal-support interactions, and modifying the support structure [18–20]. Among them, Metal-organic frameworks (MOFs) are porous materials formed through the self-assembly of metal ions and organic ligands, characterized by a high specific surface area, large porosity, and tunable pore structures [21]. MOFs featuring diverse compositions have been extensively studied for supercapacitors, electrochemical detection and catalyst synthesis [22–24]. Khan et al. [23] fabricated a VY-MOF@CNTs composite via probe sonication-assisted hydrothermal method for advanced supercapacitors. The electrochemical performance was enhanced owing to the high specific surface area and redox properties of MOFs, coupled with the conductivity of CNT network. Additionally, the related work has confirmed that the metal oxides derived from MOFs precursors possess excellent physicochemical properties, which can promote the interaction between metal/carriers and improve catalytic activity [25]. Tang et al. [26] fabricated Ce-MOF/Bi_2MoO_6 heterostructure for the photoreduction of CO_2 via the electron-coupled. They discovered that the generation of HCOOH occurred exclusively over the composites, which was attributed to the inhibition of the rapid interaction between the photoexcited electrons and CO_2-reduced intermediates. Feng et al. [27] designed a novel structure Ni/CeO_2 catalyst by immersing Ni precursor onto Ce-MOF and following by calcination. The confinement effect of MOF's porous structure resulted in high dispersion of Ni species. The Ni/CeO_2 catalyst calcined at 600 °C exhibited good stability and a high number of VOs. Liu et al. [28] explored the performance of Ni/CeO_2-MOF catalysts in dry reforming of methane by optimizing support, which effectively improved the oxygen storage and release capacity of catalyst while improving the catalytic activity and carbon deposition tolerance in high-temperature system. As aforementioned, a few studies have been conducted on the rational design of Ce-MOF materials for efficient catalytic reactions. However, the performance of Ni/CeO_2 catalysts prepared using various Ce-MOFs supports for CO_2 methanation remains extensively explored.

Based on density functional theory (DFT) calculation research contributes to providing theoretical ideas for the design of high-efficient catalysts by molecular perspective, which also can uncover the catalytic mechanism deeply. Zhang et al. [29] systematically investigated all possible reaction pathways of CO_2 methanation by DFT calculation, uncovered the intrinsic reaction mechanism over Ni/CeO_2 catalyst. Guo et al. [30] focused on the effect of loaded-metal size on the catalytic performance of the Pd-CeO_2 system for CO_2 reduction. The results demonstrated the superiority of Pd_8/CeO_2 as an electrocatalyst for the electrochemical reduction of CO_2 to CH_3OH rather than CO_2 methanation. Therefore, understanding the interaction between reaction substrates and catalytic active sites using DFT calculation is crucial to elucidate induced chemical state changes.

In this work, the MOF modification method was employed to prepare synthesize a highly dispersed catalyst for the CO_2 methanation. Easily accessible and representative Ce-MOFs (Ce-BTC, Ce-MOF-808, and Ce-UiO-66) were synthesized to serve as precursors of CeO_2. Subsequently, the Ni species were loaded onto these CeO_2 via impregnation method to prepare Ni/CeO_2 catalysts. Through the integration of experimental tools and characterization analysis, the catalytic activity and performance of Ni/CeO_2 catalyst derived from Ce-MOFs were thoroughly investigated, and using these results the influence of CeO_2 morphologies on catalytic activity was revealed. DFT calculations were also performed to study the interaction between the reaction substrate and catalyst surface, which is helpful for uncovering the catalytic mechanism deeply.

2. Experiments

2.1. Materials

Cerium (III) nitrate ($Ce(NO_3)_3{\cdot}6H_2O$), cerium (IV) ammonium nitrate, ($(NH_4)_2Ce(NO_3)_6$), 1,3,5-Benzenetricarboxylic acid (BTC), 1,4-Benzenedicarboxylic acid (BDC), methanol (CH_4O), ethanol (C_2H_6O), N,N-Dimethylformamide (DMF), and formic acid (CH_2O_2) were purchased from Macklin Biochemical Co. Ltd, Shanghai, China. Nickel nitrate ($Ni(NO_3)_2{\cdot}6H_2O$) and acetone ($(CH_3)_2CO$) were obtained from Guangdong Chemical Reagent Factory, Guangzhou, China. All Chemical materials were of analytical grade. The deionized water was supplied by Huankai Biotechnology Co. Ltd, Guangdong, China.

2.2. Catalyst preparation

2.2.1. Synthesis of Ce-MOFs

The Ce-MOF was synthesized by using methods as previously reported in the literature elsewhere with some modification [31–33]. Concretely, 2.1 g (≈0.01 mol) BTC was dissolved into 20 mL ethanol/deionized water (v: v = 1:1), and heated to 60 ℃ under water bath. Then 4.34 g (≈0.001 mmol) $Ce(NO_3)_3{\cdot}6H_2O$ was added to 45 mL of deionized water and was dropped into above solution with vigorous stirring. After being magnetically stirred for 1 h at 60 ℃. The sample was filtered and washed with ethanol and water. Finally, the collected solid was dried overnight at 70 ℃ to obtain Ce-BTC.

0.224 g BTC was dissolved into 12 mL DMF in a glass bottle, and then was the dropwise of 6 mL aqueous solution of $(NH_4)_2Ce(NO_3)_6$. Meanwhile, 2.57 mL formic acid was also added into mixture as a regulator. The mixed solution was sealed and heated for 15 min at 100 ℃. Subsequently, the glass bottle was removed cooling in a room temperature. The suspension was centrifuged and washed with DMF and acetone. Finally, the pale-yellow product was dried overnight at 70 ℃ in an oven to obtain Ce-MOF-808.

The synthesis of Ce-UiO-66 was carried out following the procedure of Ce-MOF-808, the differences were 0.531 g BDC was dissolved into 12 mL DMF in a glass bottle, instead of BTC as organic ligand, and Formic acid was not included as a regulator.

2.2.2. Synthesis of CeO_2 supports

The Ce-BTC, Ce-MOF-808 and Ce-UiO-66 were calcined at 460 °C in a Muffle furnace for 3 h. The heating rate was set at 3 ℃/min as its structure is susceptible to damage at high heating rate. To further investigate the influence of the preparation method on the catalytic performance, CeO_2 carrier was also synthesized via direct calcination. Typically, 10 g $Ce(NO_3)_3{\cdot}6H_2O$ was calcined in a muffle furnace at 500 ℃ for 6 h. Finally, the samples obtained were denoted as CeO_2-X (X = BTC, MOF-808, UiO-66 and Cal).

2.2.3. Synthesis of Ni/CeO_2 catalyst

As illustrated in Fig. 1, the schematic representation of the synthesized catalysts is presented. The active Ni species was loaded onto the support using impregnation method. A certain amount of Ni $(NO_3)_2{\cdot}6H_2O$ was dissolved in 10 mL deionized water, then added 1 g

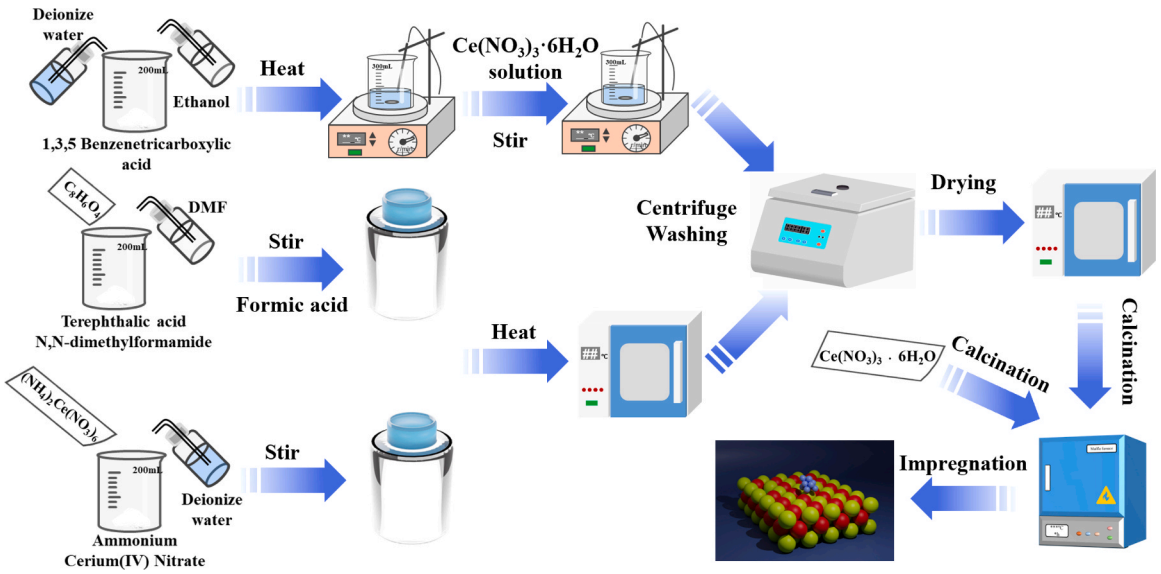

Fig. 1. Illustration of the synthesis process for the catalyst.

CeO_2-X under magnetically stirring at room temperature for 12 h. Subsequently, the sample was dried at 105 ℃ for 12 h, then calcined at 600 °C in a Muffle furnace at a heating rate of 3 ℃/min for 3 h. Finally, Ni/CeO_2 catalysts were obtained, which were defined as Ni/CeO_2-X (X = BTC, MOF-808, UiO-66 and Cal), and the nickel loading of all catalysts as 10 wt% CeO_2 derived from Ce-MOFs.

2.3. Computational details

The Vienna ab initio simulation package (VASP) [34,35] was used based on first principles in density-functional theory (DFT) calculations. The projector augmented wave (PAW) method [36] was described the core and valence electrons, and the energy cutoff of the plane-wave basis functions was set at 400 eV. The energy was calculated utilizing Generalized gradient approximation (GGA) and Perdew-Burke-Ernzerhof (PBE) exchange-correlation functional was used in all calculations [37]. The DFT + U approach is employed to characterize the 4 f electrons of Ce due to highly localized Ce 4 f orbital, with U and J values feature 5.0 and 0.5 eV, respectively [38]. The k-points in the Brillouin zone were sampled using a $1 \times 1 \times 1$ Gamma-centered Monkhorst-Pack grid for structural optimization, because of the large size of model (a=11.624307, b=11.624307, c=22.909340). The convergence tolerance was set as 1×10^{-5} eV for energy, and a maximum force criterion of 0.05 eV/Å was set for ionic relaxation.

The calculated CeO_2 lattice parameter was to be 5.479751 Å by further configuration optimization. This value is well agreement with experimental value of XRD (5.4124 Å Fm3m (225) space group) and the percentage error is 1.24 % < 5 %, which indicates the rational of calculation model and parameter (Fig. 2(a)). CeO_2 (111) was constructed by a slab model comprising 27 Ce atom and 54 O atom. A 15 Å vacuum layer in *z* direction was added to refrain the interaction of periodic image. The bottom layers were fixed (O-Ce-O), atoms in the remaining layers, as well as Ni cluster and adsorbates were completely

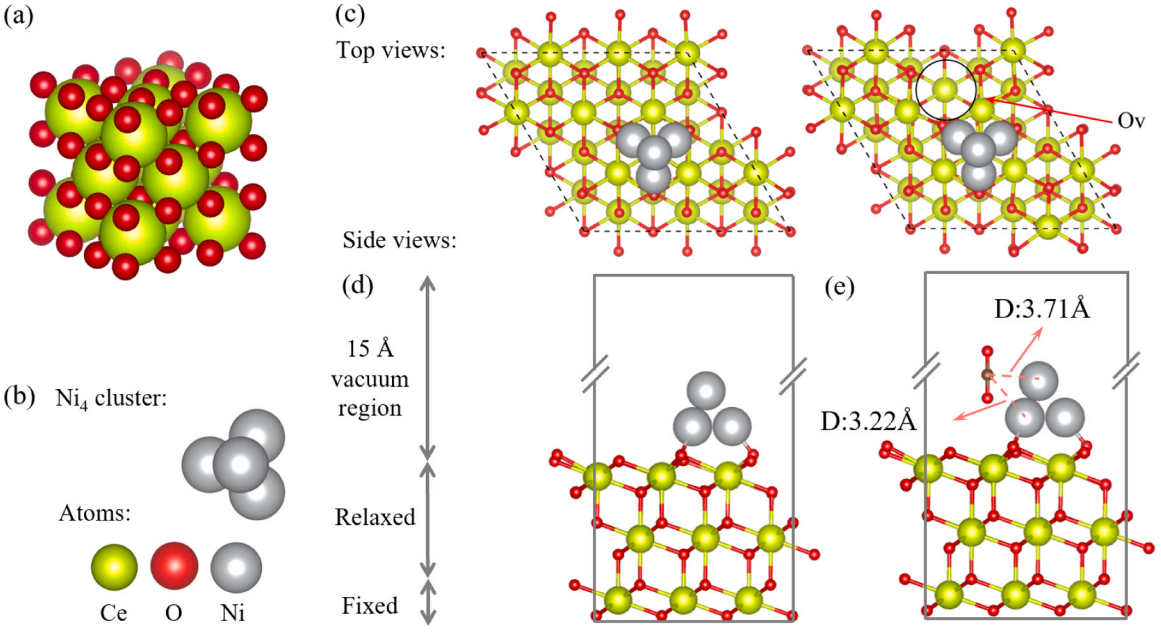

Fig. 2. (a) CeO_2 conventional cell; (b) Ni_4 clusters; (c) $Ni_4/CeO_2(111)$-Perfect/Defect- Optimized; (d) Initial adsorption model of $Ni_4/CeO_2(111)$-Perfect/Defect.

relaxed. The CeO_2-supported Ni species was simulated as Ni_4 cluster on the CeO_2 (111) surface. (see Fig. 2(b) and (d))

To investigate CO_2 adsorption behavior at perfect and defect crystal surface of Ni_4/CeO_2, the molecule was placed in the surface of catalyst with approximately 2.5 Å of distance, as shown in Fig. 2(c), (e). The adsorption energy (ΔE_{ads}) estimates by the Eq. (2) [30]:

$$\Delta E_{ads} = E_{slab/adsorbate} - E_{slab} - E_{adsorbate} \quad (2)$$

where $E_{slab/adsorbate}$, E_{slab} and $E_{adsorbate}$ are respectively the total energy of the adsorbed system, total energy of pure catalyst surface and total energy of adsorbed molecule.

2.4. Catalyst characterization

X-ray diffraction (XRD) was used to identify the crystal structure of the catalyst, employing Cu-Kα radiation (λ = 1.5418 Å) on a Rigaku Smartlab instrument (Rigaku, Japan). The *2θ* scanning range was from 10° to 80°, with a scanning rate of 3°/min. The metal Ni loading amount for all fresh catalysts was carried out using Agilent ICP-OES 720 ES spectrometer. Nitrogen (N_2) physical adsorption-desorption measurements were performed to determine the pore structure on a 3Flex physical adsorption instrument (Micromeritics, America). The specific surface area and pore size were calculated by Brunauer-Emmet-Teller (BET) and Barrett-Joyner-Halenda (BJH) methods. Transmission electron microscopy (TEM) and high-resolution TEM (HRTEM) analysis were carried out on a JEM-1400Flash (JEOL, Japan), with Energy-Dispersive X-ray spectroscopy (EDS) also performed on the same instrument. X-ray photoelectron spectroscopy (XPS) measurements were conducted on a Thermo K-Alpha instrument (Thermo Fisher Scientific, America). Raman spectra were conducted on LabRAM Odyssey (Horiba Scientific) instrument. The basicity of the reduced catalysts was determined using CO_2-TPD on TP-5080 (Xianquan, China) instrument. Typically, certain sample was first heated in pure He at 300 ℃ for 1 h. The CO_2 was injected (30 mL/min) for 1 h after the sample was cooled to 50 ℃. Next, the He (30 mL/min) was used for purging, and the temperature was increased to 800 ℃ at 10 ℃/min.

2.5. Catalytic activity measurements

The thermal CO_2 reduction test was conducted in a quartz tube reactor (inner diameter = 14 mm). Internal and external mass diffusion effects were ruled out via pre-experiments prior to assessing catalytic performance. In each test, 50 mg of the catalyst (100 mesh) was placed in the constant temperature zone of the reactor and heated in a 60 mL/min pure N_2 to the desired reduction temperature (600 ℃). The catalyst was reduced *in situ* in 60 mL/min H_2/N_2(volume ratio H_2:N_2=1:4) for 1 h. Then, the reactor was cooled to 200 ℃ under a N_2 atmosphere at the same flow rate. Subsequently, the reaction gases (volume ratio CO_2:H_2:N_2=1:4:15) were introduced. Once the reaction time and temperature specified in the protocol were reached, the emitted gases were analyzed by a gas chromatograph to evaluate CO_2 reduction reaction. The conversion of CO_2 (X_{CO_2}), selectivity of methane (S_{CH_4}) and product yield (Y_X) were calculated using the following formulas.

$$X_{CO_2} = \frac{(F_{CO_2,in} - F_{CO_2,out})}{F_{CO_2,in}} \times 100\% \quad (3)$$

$$S_{CH_4} = \frac{F_{CH_4,out}}{(F_{CO_2,in} - F_{CO_2,out})} \times 100\% \quad (4)$$

$$Y_{CH_4} = \frac{F_{CH_4,out}}{m_{cat}} \quad (5)$$

where $F_{CO_2,in}$ and $F_{CO_2,out}$ are the molar flow rates of CO_2 at inlet or outlet, $F_{CH_4,out}$ and$F_{CO,out}$ represent are the volume flow rates of CH_4 and CO at outlet.

3. Results and discussion

3.1. Catalytic CO_2 reduction performance

The CO_2 reduction tests over Ni/CeO_2-X catalysts were conducted at ambient pressure, with temperatures ranging from 200 to 450 ℃ and a WHSV of 72,000 mL·g_{cat}^{-1}·h^{-1}. As depicted in Fig. 3(a), the CO_2 conversion curves were initially increased with the rising temperature from 200 to 400 ℃ for all catalysts and gradually approached the predicted-equilibrium values, which can be assigned to the exothermic nature of the Eq. (1). While increasing the temperature to 400 °C resulted the best CO_2 conversion for all samples, the boost was only 0.1–1.2 % compared with 375 °C, showing no significant improvement. Thus, the optimal reaction temperature is 375 °C. It can be clearly seen that CO_2 conversion for Ni/CeO_2-BTC was higher than the others under the identical condition and reached 61.9 % at 375 ℃. Noteworthily, the temperature exerts a negative effect on CO_2 conversion at 400–450 ℃, particularly Ni/CeO_2-Cal. This shift stems from the metal Ni being prone to aggregation at higher temperatures. However, the CO_2 conversion of Ni/CeO_2 catalysts derived from Ce-MOFs remained nearly unchanged, suggesting enhanced anti-agglomeration ability under higher temperatures. Moreover, all catalysts produce CH_4 as the primary product. In comparison with other catalysts, the Ni/CeO_2-Cal catalyst exhibits higher CH_4 selectivity in the lower temperature range, but its selectivity significantly drops within 300–400°C. Excepting Ni/CeO_2-Cal catalyst, the selectivity for CH_4 over Ni/CeO_2-X exceeds 85 % in the reaction temperature window of 300–400 ℃, slightly lower than the reported values (Table 1). The variation can be attributed to the reactants/intermediates failing to be adsorbed and converted promptly on catalyst surface at higher WHSV, leading to poor selectivity [11,39]. The CH_4 yield for all obtained catalysts were presented in Fig. 3(c). The CH_4 yield from the Ni/CeO_2-BTC catalyst maintains the most superior in the present study, with generation rates of 0.086 mol·g_{cat}^{-1}·h^{-1}.

Additionally, the catalytic stability of Ni/CeO_2-BTC was further assessed by performing continuous CO_2 methanation over 24 h at the optimal reaction temperature of 375°C (see Fig. 3(d)). During the 24 h time on stream (TOS), the CO_2 conversion displayed only a minor decline, from an initial 60.1–59.6 %, while CH_4 selectivity remained consistently more than 85 %. This underscores the reliable catalytic stability of Ni/CeO_2-BTC. A comparison of the catalyst performance with data from published literature was provided in Table 1. The catalytic performance of Ni based catalysts manifest a substantial difference due to the variation in loading of active species and WHSV conditions. As for the synthesized Ni/CeO_2 catalysts derived from Ce-MOFs in present study, the CO_2 conversion was relatively promoted compared with the reported catalysts in higher WHSV.

3.2. Catalyst characterization

The XRD patterns obtained for the different Ce-MOFs are shown in Fig. 4. All samples were in the form of microcrystalline powders. In Fig. 4(a), all observed peaks of Ce(1,3,5-BTC)$(H_2O)_6$ were closely related to the known bulk phrase La(1,3,5-BTC)$(H_2O)_6$ [44]. The strong peak and peak positions clearly indicate the good crystallinity of Ce-MOFs. The crystal structure of Ce-BTC with space group Cc, involved Ce atom, 1,3,5-H_3BTC ligands and water molecules. The cluster unit of synthesized Ce-MOF-808 with Fd-3m space group was composed by OH^-, H_2O and BTC^{3-} linkers (Fig. 4(b)), with final in the formula $[Ce_6(\mu_3\text{-}O)_4(\mu_3\text{-}OH)_4(BTC)_2(OH)_6(H_2O)_6]$. And it featured a 3,6-connected three-dimensional framework with spn topology [33]. As for Ce-UiO-66 in Fig. 4(c), it was constructed from $[Ce_6O_4(OH)_4]^{12+}$ clusters and BDC^{2-} linkers, with final in formula $[Ce_6O_4(OH)_4(BDC)_6]$ and crystallizing in space group Fm-3m [33]. As depicted in Fig. 4, the experimental data exhibits good consistency with the simulation results, supporting the successful synthesis of Ce-MOFs.

The metal Ni weight of the as-prepared catalysts was measured by

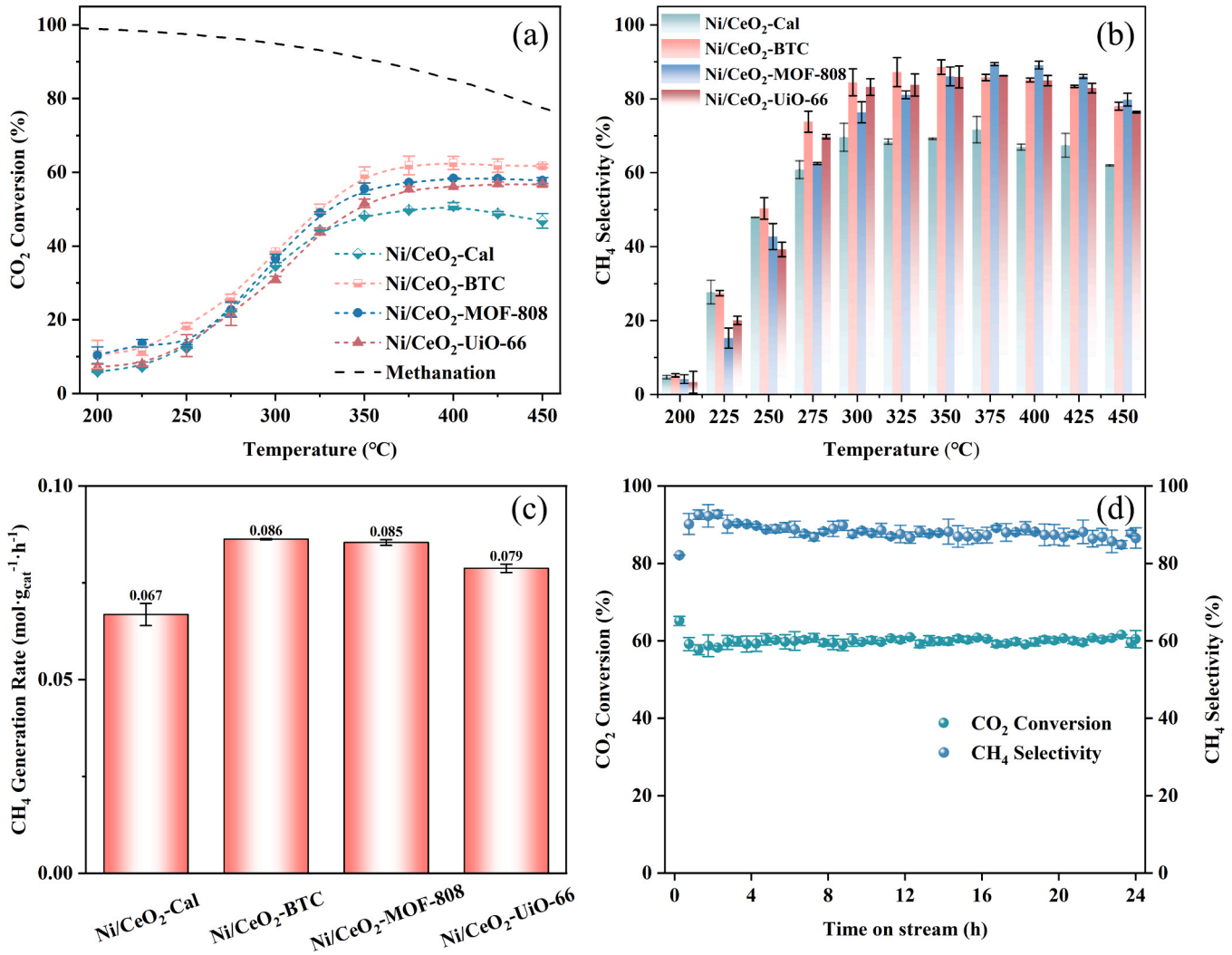

Fig. 3. The CO_2 reduction performance over Ni/CeO_2-X catalysts (a) CO_2 Conversion; (b) CH_4 Selectivity; (c) CH_4 Yield; (d) The stability test for CO_2 methanation at 375 °C for 24 h. (Reaction conditions: T = 375 °C, P = 1 atm, WHSV = 72,000 mL·g_{cat}^{-1}·h^{-1}).

Table 1
Comparison of catalytic activity between various Ni catalysts for CO_2 methanation.

Catalyst	*Temperature (°C)*	*WHSV (mL·g_{cat}^{-1}·h^{-1})*	*CO_2 Conversion (%)*	*CH_4 Selectivity (%)*	*Ref*
10 wt% Ni/CeO_2-SG	300	30,000	70	98	[40]
20 wt% Ni/CeO_2-SGM	250	10,000	82.5	94.8	[41]
Ni/SiO_2	450	12,000	80	88	[11]
Ni/ZrO_2	350	60,000	50.2	100	[12]
10 wt% Ni/CeO_2	300	22,000	84.1	100	[15]
20 wt% Ni-HT	400	5,000	83.5	97	[39]
15 wt% Ni/CeO_2	350	45000	82	96	[42]
10 % Ni/CeO_2	250	14,000	42	100	[43]
Ni/CeO_2-BTC	375	72,000	61.9	86	This work
Ni/CeO_2-MOF−808	375	72,000	57.3	89	This work
Ni/CeO_2-UiO−66	375	72,000	55.4	85	This work

ICP-OES (Table S1). The real Ni content closely matches the theoretical value. The XRD patterns obtained for the Ni/CeO_2-X catalysts derived from different Ce-MOFs are shown in Fig. 5. The diffraction peaks observed at 2θ = 28.53, 33.05, 47.48, 56.35, 59.08829, 69.37, 76.76, and 79.08 ° ascribe to (111), (200), (220), (311), (222), (400), (331), and (420) crystal facets of CeO_2 (ICDD PDF No.81–0792) with space group Fm3m (225), which agrees well with those previous studies in the literature [45,46]. No significant variations in diffraction peaks were observed across CeO_2 originating from different Ce-MOFs. The diffraction peaks with relatively high intensity indicate good crystallinity of CeO_2 in the prepared catalysts. For fresh catalysts, three weak characteristic peaks at 2θ = 37.28, 43.32, and 62.93 °, corresponding to the (111), (200), and (220) crystal faces of NiO phase, respectively [20]. This result could be attributed to the high dispersion and the low contents of Ni metals on CeO_2 support resulted by special structure of Ce-MOFs. Furthermore, as shown in Fig. 5(b), the crystal faces (111), (200), and (220) of Ni (ICDD PDF No.87–0712) are detected at 2θ = 45.50, 51.11, and 78.37 °, respectively. The weaker peak of

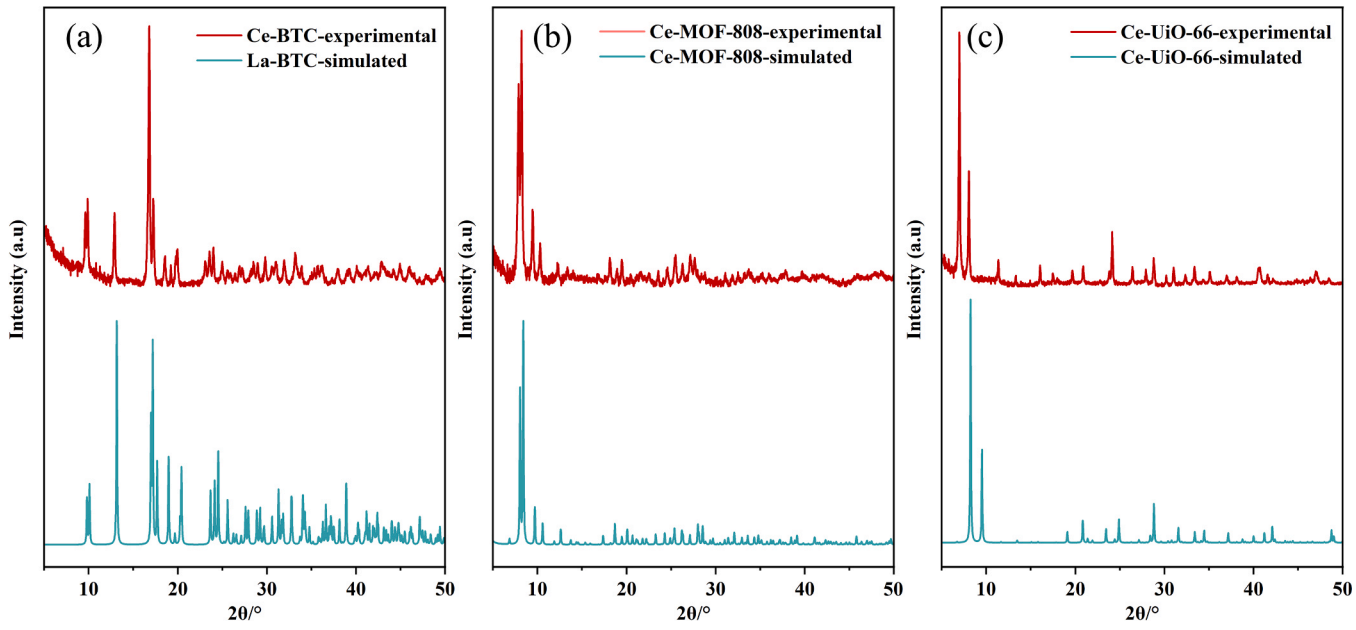

Fig. 4. XRD patterns obtained for the Ce-MOFs (a) Ce-BTC; (b) Ce-MOF-808; (c) Ce-UiO-66.

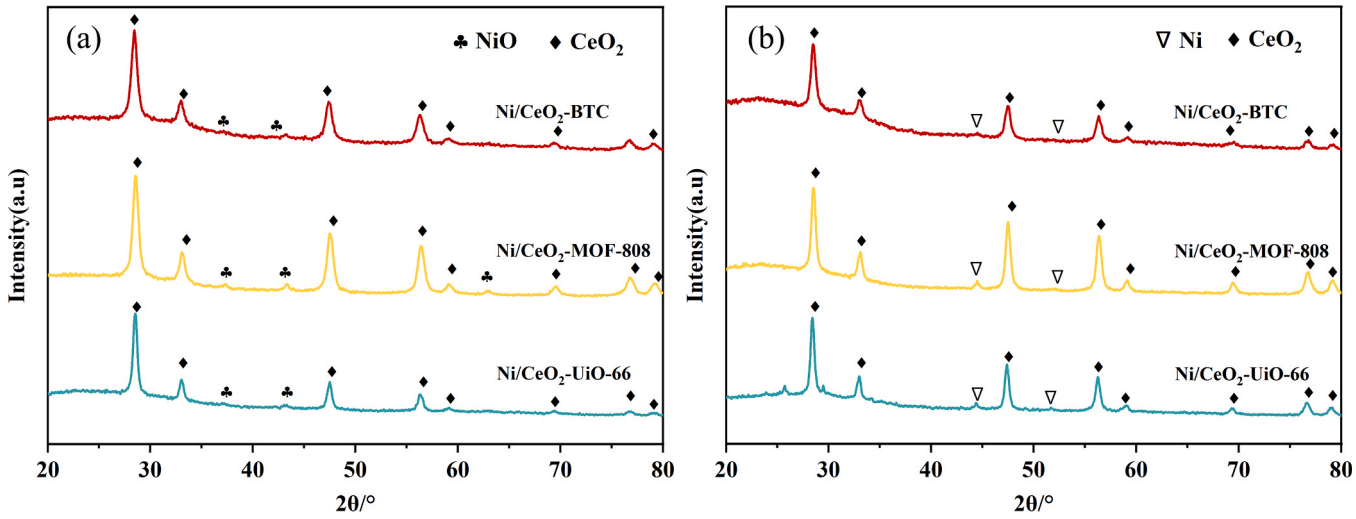

Fig. 5. XRD patterns obtained for the Ni/CeO_2-X catalysts derived from Ce-MOFs (a) fresh and (b) reduced.

Ni/CeO_2-BTC at $2\theta = 45.50^\circ$ compared to the other catalysts suggests a more uniform distribution of Ni species on the support, which is a primary reason contributing to its superior catalytic activity observed in CO_2 reduction tests. Based on the Debye–Scherrer equation, the average grain sizes of the CeO_2 for all catalysts are presented in Table 2. The average crystalline size of CeO_2 increases upon completion of hydrogen reduction process, with the Ni/CeO_2-BTC catalyst exhibiting the smallest size. The small average crystalline boosts the specific surface area and pore volume of the catalyst, thereby improving catalytic activity [47].

The N_2 adsorption-desorption curves obtained for the reduced Ni/CeO_2-X catalysts derived from different Ce-MOFs are illustrated in Fig. 6 and Table 2 displayed supplementary contents. Fig. 6(a) shows a typical V isotherm obtained for the Ni/CeO_2-X catalysts with a H3-type hysteresis loop, such as Ni/CeO_2-BTC and Ni/CeO_2-UiO-66, which implies the presence of slit-like pores [47]. While, Ni/CeO_2-BTC catalyst possesses a type IV isotherms with H4-type hysteresis loop, indicating the mesoporous structure [48]. Compared to the fresh Ni/CeO_2-X in Fig. S1, the type of adsorption curve remained unchanged. Also, as observed in

Table 2
Texture properties of the Ni/CeO_2-X catalysts derived from different Ce-MOFs.

Samples	*Surface area* ($m^2 \cdot g^{-1}$)	*Total pore volume* ($cm^3 \cdot g^{-1}$)	*Average pore diameter (nm)*	*CeO_2 grain size (nm)*[c]
Ni/CeO_2-BTC[a]	44.43	0.32	28.62	13.11
Ni/CeO_2-MOF−808[a]	36.98	0.09	10.09	12.81
Ni/CeO_2-UiO−66[a]	26.92	0.13	19.27	16.26
Ni/CeO_2-BTC[b]	38.98	0.24	24.83	15.08
Ni/CeO_2-MOF−808[b]	31.63	0.08	9.89	15.74
Ni/CeO_2-UiO−66[b]	27.33	0.13	18.90	19.89

[a] Fresh.
[b] Reduced.
[c] Calculated by XRD patterns.

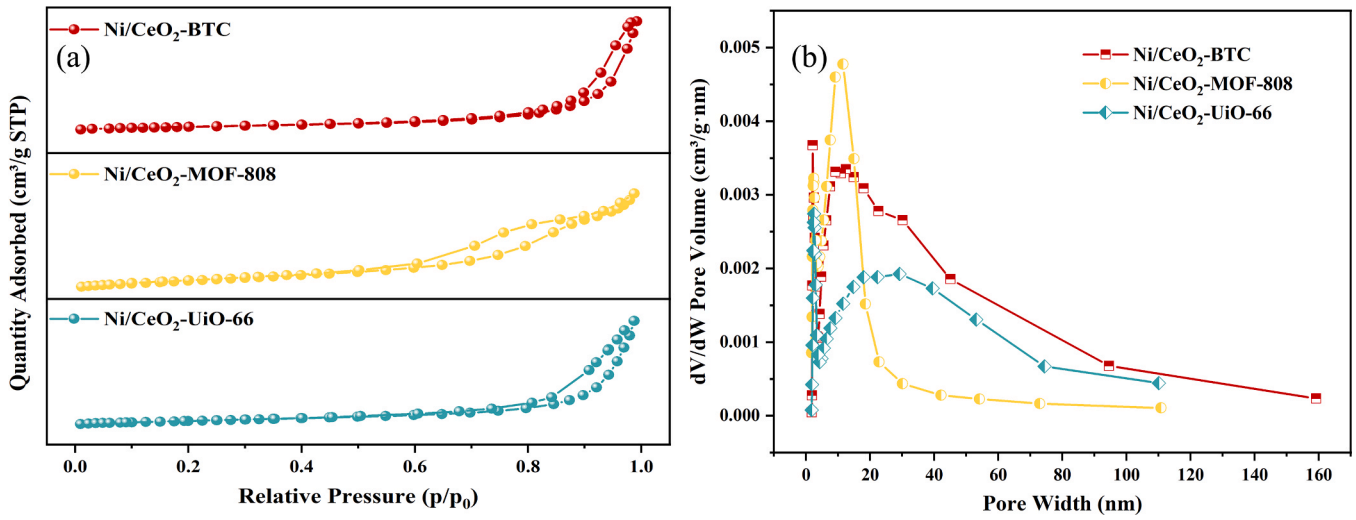

Fig. 6. N_2 adsorption-desorption curves (a) and pore size distribution (b) obtained for the reduced Ni/CeO_2-X catalysts.

Fig. 6(b), the pore size distribution of all simples is not regular and primarily ranges from 2 to 70 nm, encompassing both the mesopores (2–50 nm) and macropores regions (>50 nm). And the differences in pore size of the catalysts likely influence the adsorption and dissociation of CO_2, thereby resulting in different performance of CO_2 to methane [39].

From the results in Table 2, the BET specific surface areas for the reduced catalysts follow the order: Ni/CeO_2-BTC>Ni/CeO_2-MOF-

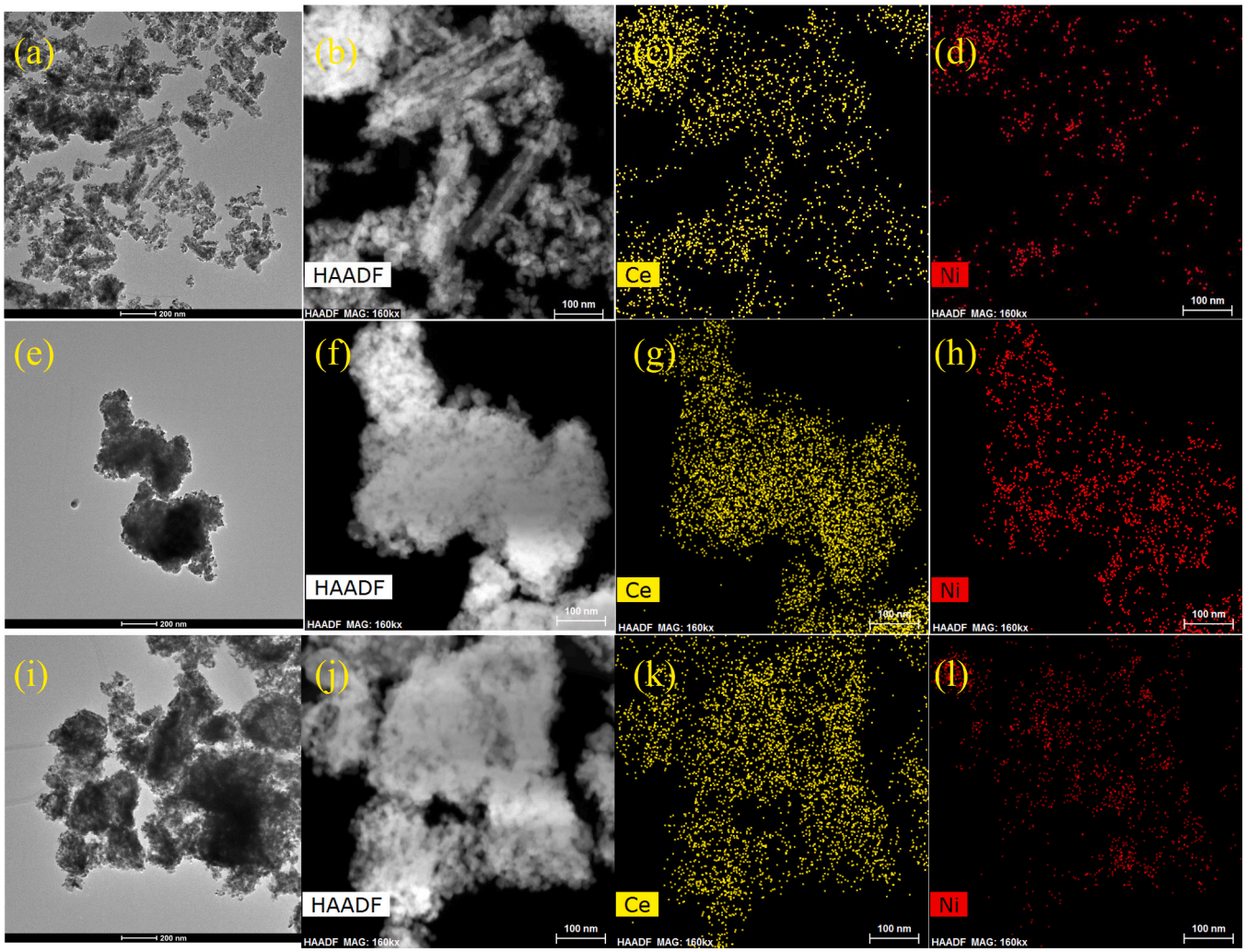

Fig. 7. TEM images obtained for the reduced Ni/CeO_2-X catalysts, (a, e, i) Ni/CeO_2-BTC, Ni/CeO_2-MOF-808, Ni/CeO_2-UiO-66 and corresponding EDS mapping of Ce (c, g, k) and Ni (d, h, l).

808 >Ni/CeO_2-UiO-66. Compared with Ni/CeO_2-MOF-808 and Ni/CeO_2-UiO-66, Ni/CeO_2-BTC still has highest specific surface areas and average pore diameters with values of 38.98 $m^2 \cdot g^{-1}$ and 24.83 nm. Furthermore, Ni/CeO_2-BTC has two peaks, the wide peak between 5 and 50 nm means more pores and the peak at 3–5 nm is narrower, meaning more uniform, and the highest peak at approximate 3 nm indicates more pores of this pore size. Generally, better pore structure favors the gaseous reactants adsorption and diffusion as well as the activation of intermediate products [42]. Also, based on the literature, CO_2 adsorption and dissociation occurred on the surface of catalyst is the first step in CO_2 reduction [49]. Consequently, the Ni/CeO_2-BTC catalyst having superior specific surface area, pore volume and pore size help to better Ni metal particles dispersion and then enhance the adsorption and dissociation of CO_2, which corresponds with the results of XRD.

The surface morphology and structure of the reduced Ni/CeO_2-X catalysts observed by transmission electron microscopy (TEM) to reveal the morphological discrepancies of samples, and the results are summarized in Fig. 7. The irregular shape may be attributed to the CeO_2 support being observed on a brighter background. The smaller and blacker regions are assigned to metallic Ni particles on the surface or in mesoporous of Ni/CeO_2-X. It is a well-documented fact that rod-like structure of Ni/CeO_2-BTC has lower reduction temperature, causing an excellent performance in CO_2 reduction [42]. Also, it can be observed that the reduced Ni/CeO_2-BTC still maintains a rod-like shape contrasted with the fresh in Fig. S2 [50]. By contrast, Ni/CeO_2-MOF-808 and Ni/CeO_2-UiO-66 exhibits similar octahedral structure as shown in Fig. 8 (HRTEM) maintaining their original shapes (Fig. S3) [51]. In Fig. 8, the lattice fringes reflect the interplanar distance of about 0.20 nm corresponding to Ni (111) plane. The crystal face (111) of Ni element is generally believed to possess high catalytic activity in CO_2 hydrogenation to methane [39]. CeO_2 support is dominated by (111) plane, and the lattice fringes distance is around 0.31 nm. The crystal face results of this part demonstrate consistency with XRD analyses.

EDS semi-quantitative analysis confirmed Ni existed and effectively loaded on CeO_2 support derived from various Ce-MOFs. Elemental mapping in Fig. 7(d), (h), (l) further revealed that active Ni particles on the reduced Ni/CeO_2-BTC catalyst exhibited more uniform dispersion, as evidenced by the nickel element (red) being predominantly distributed in area without Ce (yellow), compared to other catalysts. This not only enhanced homogeneity effectively mitigates Ni phase agglomeration, but also contributing to the formation of metal-support interface, highlighting the structural advantage of the Ni/CeO_2-BTC system [11].

The surface properties of the reduced Ni/CeO_2-X were conducted by XPS profiles and the characterization results shown in Fig. 9. The Ce 3d region can be deconvoluted into 10 characteristic peaks. The characteristics peaks labeled u_1 (~882.5), u_3 (~887.1 eV), v_1 (~898.4 eV), and v_3 (~901.1 eV) exhibit the Ce^{3+} species of Ce_2O_3 while the remaining six characteristics peaks, namely u_2 (~885.4 eV), u_3 (~890.3 eV), v_0 (~899.9 eV), v_2 (~903.2 eV), v_4 (~908.8 eV) and u_4 (~918.5 eV) are corresponded to the Ce^{4+} species of CeO_2 [41]. The existence of Ce^{3+} usually leads to the formation of oxygen vacancies in it. Furthermore, the simultaneous presence of Ce^{3+} and Ce^{4+} in all reduced Ni/CeO_2-X samples was affirmed, as a consequence, favoring for the cycling of oxygen species on catalyst surface [46].

The O1s spectra of the reduced Ni/CeO_2-X catalysts were also investigated to obtain information about oxygen vacancies. Generally, oxygen vacancies on an oxide catalyst as valuable reactive sites could affect deeply in several catalytic reaction [52]. Fig. 9 exhibits three

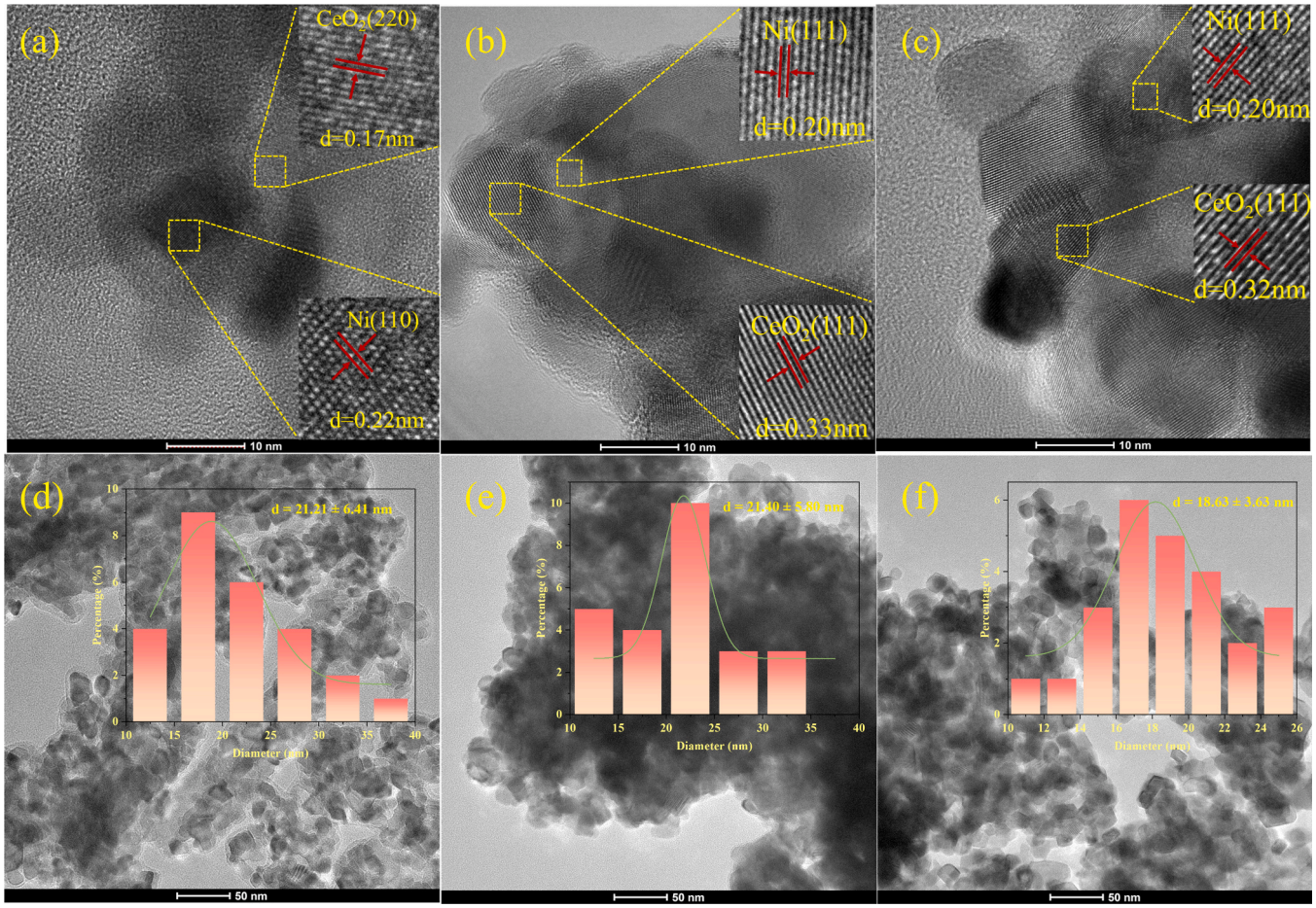

Fig. 8. HRTEM images obtained for the reduced Ni/CeO_2-X catalysts, (a, d) Ni/CeO_2-BTC, (b, e) Ni/CeO_2-MOF-808, (c, f) Ni/CeO_2-UiO-66.

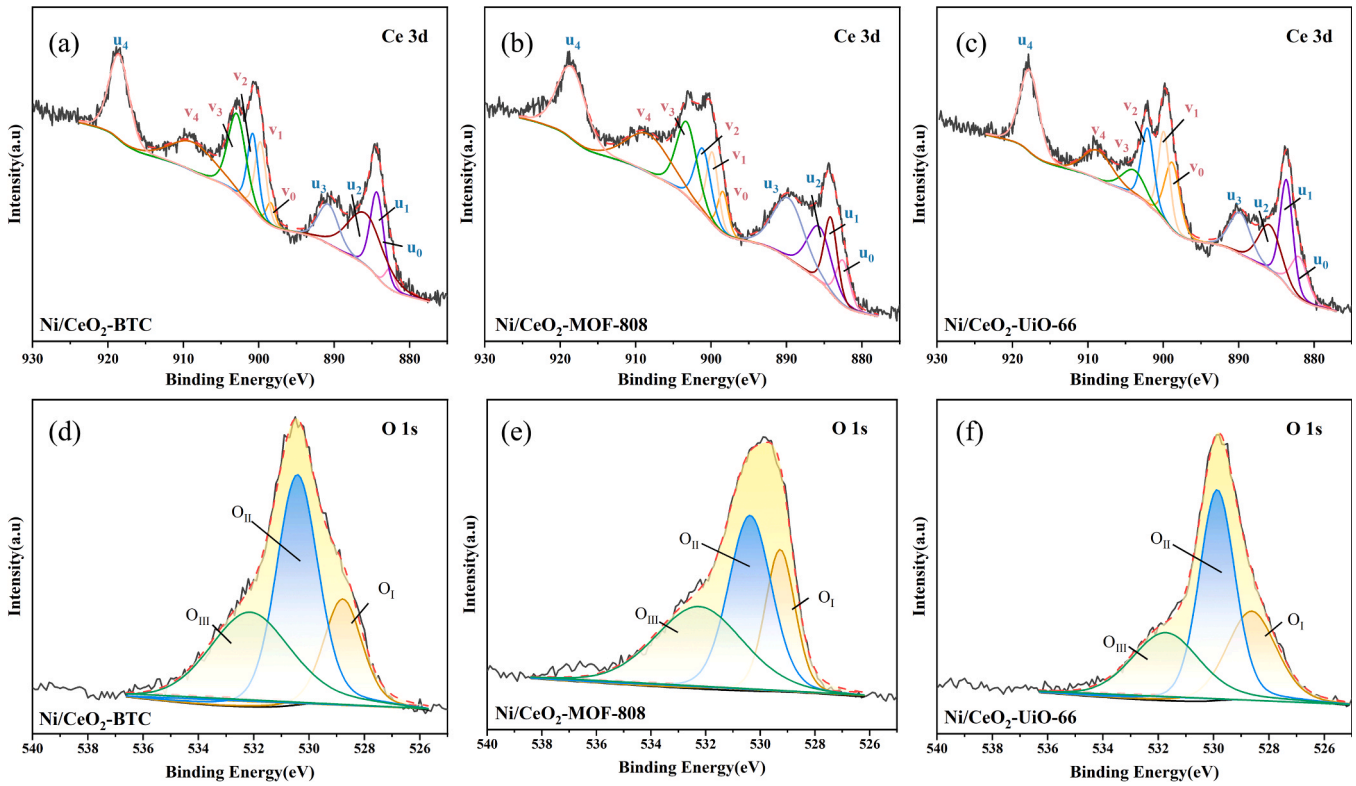

Fig. 9. XPS spectra obtained for the reduced Ni/CeO_2-X catalysts, (a, b, c) Ce 3d, (d, e, f) O 1 s.

characteristic peaks of O1s, which can be assigned to lattice oxygen O_I (~528.8 eV), oxygen vacancy O_{II} (~530.4 eV) and surface adsorbed oxygen O_{III} (~532.1 eV) [20,53]. Usually, oxygen vacancies play a key role in activating CO_2. Table 3 shows the proportion of $O_{II}/(O_I + O_{II} + O_{III})$ from fitting peak area of all catalysts. Calculations indicate that the reduced Ni/CeO_2-BTC has the highest $O_{II}/(O_I + O_{II} + O_{III})$ ratios, so it implies more oxygen vacancies amounts. The above results show that CeO_2 derived from various MOFs has a major impact on the content of oxygen vacancies.

In comparison to the fresh catalysts (Fig. S4 and Table. S2), the binding energies of Ce and O elements remained largely unchanged across all catalysts (the fresh and reduced). However, a marked increase in oxygen vacancy concentration was observed specifically in Ni/CeO_2-BTC and Ni/CeO_2-MOF-808. This phenomenon is likely attributable to its unique microstructural features, which may facilitate enhanced defect formation.

Table 3
Surface composition of the reduced Ni CeO_2-X catalysts calculated by their XPS results.

Catalyst	*Ce (eV)*		*O (eV)*			
	Ce^{3+}	Ce^{4+}	O_I	O_{II}	O_{III}	$O_{II}/(O_I + O_{II} + O_{III})$
Ni/CeO_2-BTC	882.5, 885.9 898.4, 900.8	884.3, 890.7 899.8, 902.9 908.7, 918.5	528.8	530.4	532.1	0.45
Ni/CeO_2-MOF−808	882.5, 885.7 898.4, 901.1	884.1, 889.7 899.8, 903.2 908.3, 918.5	529.3	530.4	532.2	0.39
Ni/CeO_2-UiO−66	882.0, 885.9 898.7, 901.9	883.7, 889.8 899.9, 903.7 908.6, 917.8	528.6	529.9	531.7	0.44

The oxygen vacancy information of the reduced Ni/CeO_2-X catalysts were recorded by Raman spectra, as illustrated in Fig. 10(a). All three samples exhibit a stronger peak at 460 cm-1, caused by the local octahedral symmetry vibration of CeO_2 lattice (F_{2g}) [41,53]. The F_{2g} peak shifts to lower wavenumbers compared to pure CeO_2, which arises from the oxygen vacancy in Ni/CeO_2 catalyst derived from Ce-MOFs. A weak peak at 560 cm^{-1} may ascribe to the Ni-induced extrinsic oxygen vacancies in CeO_2, and the characteristic peak at 590 cm^{-1} belonged to vibration peak caused by surface defect-induced mode of CeO_2 (F_D) [54]. As aforementioned these features, verifying the generation of oxygen vacancy.

The basic strength and basicity site density obtained for the Ni/CeO_2-X catalysts derived from Ce-MOFs were evaluated by CO_2-TPD, as depicted in Fig. 10(b) and Table 4. The CO_2 desorption peaks (<320 ℃) corresponded to the weak basic site. These peaks are typically associated with -OH groups and other oxygen species arising from weakly adsorbed oxygen on surface oxygen vacancies or Ni-O-Ce interfacial sites, where CO_2 is adsorbed in the form of bicarbonates [18,19]. The broad peaks (320–730 ℃) were medium basic site resulting from the Lewis alkali on metal oxides, primarily due to the decomposition of bidentate carbonates [55]. The peaks (>730 ℃) were attributed to strong basic site namely the O^{2-} anions as Lewis basic sites [56]. The CO_2 desorption curves of all samples were divided into three temperature regions including 50 −320 °C, 320 −730 °C and 730 −800 °C, respectively. The CO_2 adsorption sites for the three catalysts are mainly composed of weak and medium basic sites, especially the weak basic site. The reported studies have manifested weak and medium basic sites are more favorable for the performance of CO_2 adsorption and activation than strong alkali sites[19,56]. While strong basic sites adverse to desorb the intermediate species/reactants [56]. Distinctly, despite possessing fewer effective basic sites than others, Ni/CeO_2-BTC catalyst achieved the

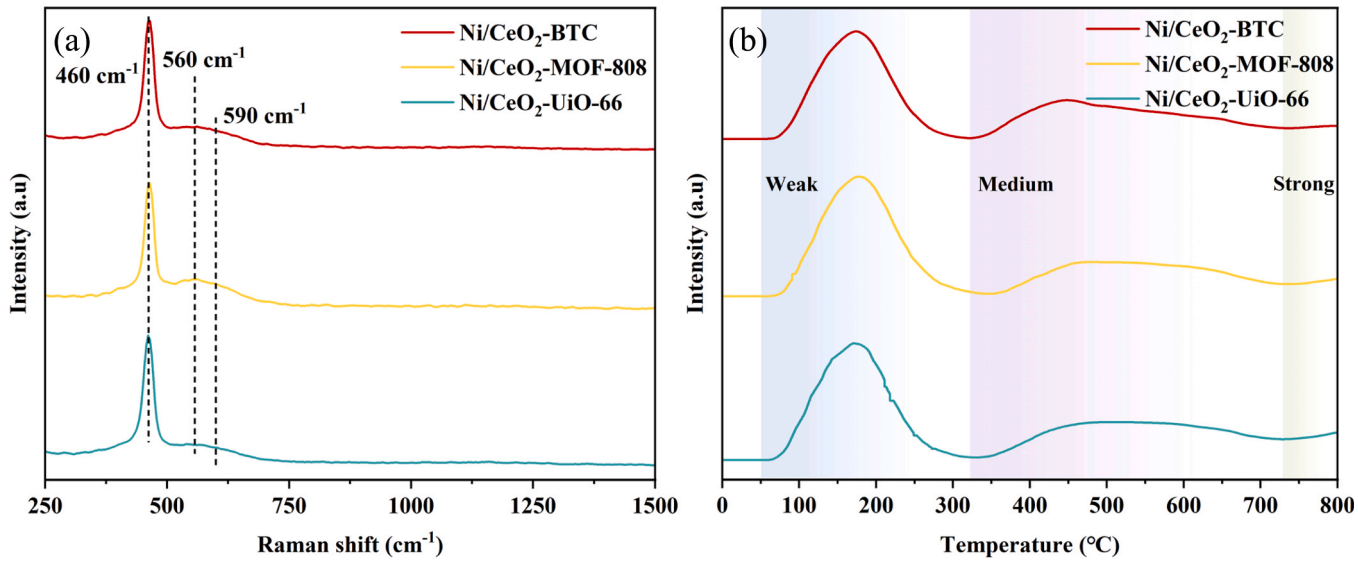

Fig. 10. Raman and CO_2-TPD profiles obtained for the reduced Ni/CeO_2-X catalyst, (a) Raman spectra, (b) CO_2-TPD.

Table 4
Basic sites on the Ni/CeO_2-X catalytic surface.

Catalyst	*Temperature range (℃)*	*CO_2 desorbed (mmol·g^{-1})*	*Effective basic sites (mmol·g^{-1})*[a]	*Total (mmol·g^{-1})*
Ni/CeO_2-BTC	50–320	0.165	0.295	0.306
	320–730	0.130		
	730–800	0.011		
Ni/CeO_2-MOF−808	50–320	0.190	0.318	0.331
	320–730	0.128		
	730–800	0.013		
Ni/CeO_2-UiO−66	50–320	0.121	0.223	0.238
	320–730	0.102		
	730–800	0.015		

[a] Effective basic site = Weak basic site (50–320 ℃) + Moderate basic site (320–730 ℃).

highest CO_2 conversion under identical conditions, suggesting that basic strength alone is not unique factors for catalytic activity. Lastly, based on those results in present paper, the CO_2 conversion of different catalysts was analyzed in relation to their specific surface area, oxygen vacancies, and total base density, as illustrated in Fig. S8. Results show that the CO_2 conversion of Ni/CeO_2 catalysts derived from Ce-MOFs exhibits only linearly related to the specific surface area of the catalyst, with no linear relationship observed for other factors. This discrepancy may stem from variations in catalyst morphology.

3.3. Molecular simulation models and DFT studies

Based on the results of XRD and according to XPS profiles for the reduced Ni/CeO_2-BTC catalyst, the oxygen vacancy resulted in the shift between Ce^{3+} and Ce^{4+} was to be formed in those catalysts. Also, CeO_2 (111) is the most easily exposed plane in our present work, which also means it has abundant oxygen vacancies, as well as indicating this crystal facet demonstrates greater potential for effective loading of active Ni species. Further DFT calculations on the reactant's adsorption at the surface of catalyst were carried out using Ni_4/CeO_2 (111). The adsorbed CO_2 serves as a prerequisite for the subsequent reactions continuing. The oxygen vacancy formation energies (E_{vac}) are calculated by the Eq. (6):

$$E_{vac} = E_{def} - E_{per} + 1/2E_{O_2} \quad (6)$$

where*Edef*is the defect model energy,*E*peris the perfect model energy,*EO*$_2$is the free oxygen molecule energy.

The vacancy formation energy for the Ni_4/CeO_2 (111) surface generating one oxygen vacancy was calculated to be 2.5 eV, which is a similar value with the results of Yang et al. [57]. Seen from the optimized configurations of Ni_4/CeO_2 (111) in Fig.11(a), three Ni atoms interact with O atoms from CeO_2 (111) surface, suggesting that CeO_2 (111) stabilizes Ni_4 clusters.

As being critical initial step in the hydrogenation process, the adsorption of CO_2 on the Ni_4/CeO_2 (111) surface was investigated in this work. The CO_2 adsorption at site 1 was presented as depicted in Fig. 2(d) and Fig. 11(b). For the perfect and defect Ni_4/CeO_2 (111), CO_2 molecule tilts from a perpendicular orientation to approximately 45° relative to the surface. However, the ΔE_{ads} were extremely low, only −0.039 eV and −0.047 eV respectively (Fig. S5(c)). The difference in ΔE_{ads} suggested that defective Ni_4/CeO_2 (111) was more favorable for CO_2 adsorption and C═O bond activation by serving as the Lewis basic site for CO_2 adsorption [57]. Based on this case, subsequent calculations for some possible initial adsorption sites on the defective surface were carried out. The ΔE_{ads} for these sites were listed in Fig. 11(c), it was found that strong chemisorption of CO_2 in sites 2, site 3 and sites 4 was shown, while site1 only was a physisorption process. And the highest ΔE_{ads} of CO_2 on Ni_4/CeO_2 (111) was at site 4 (-0.77 eV), where CO_2 adsorption at the interface of Ni-O-Ce. The ΔE_{ads} of site 2 and site 3 ranged from −0.64 eV to 0.66 eV (i.e., close with each other), where CO_2 adsorbed at the edge and vertex of the cluster respectively. The largest ΔE_{ads} at site 4 compared with other sites can be attributed to the influence exerted on CO_2 molecular by both supported Ni atoms and the CeO_2 (111) surface O atoms.

For site 4 (Fig. 11(b) and Table 5), the C═O bond length elongated to 1.29 Å without cleavage, and C atom approached CeO_2 (111) surface O atom, causing the destruction of initial CO_2 configuration from linear to

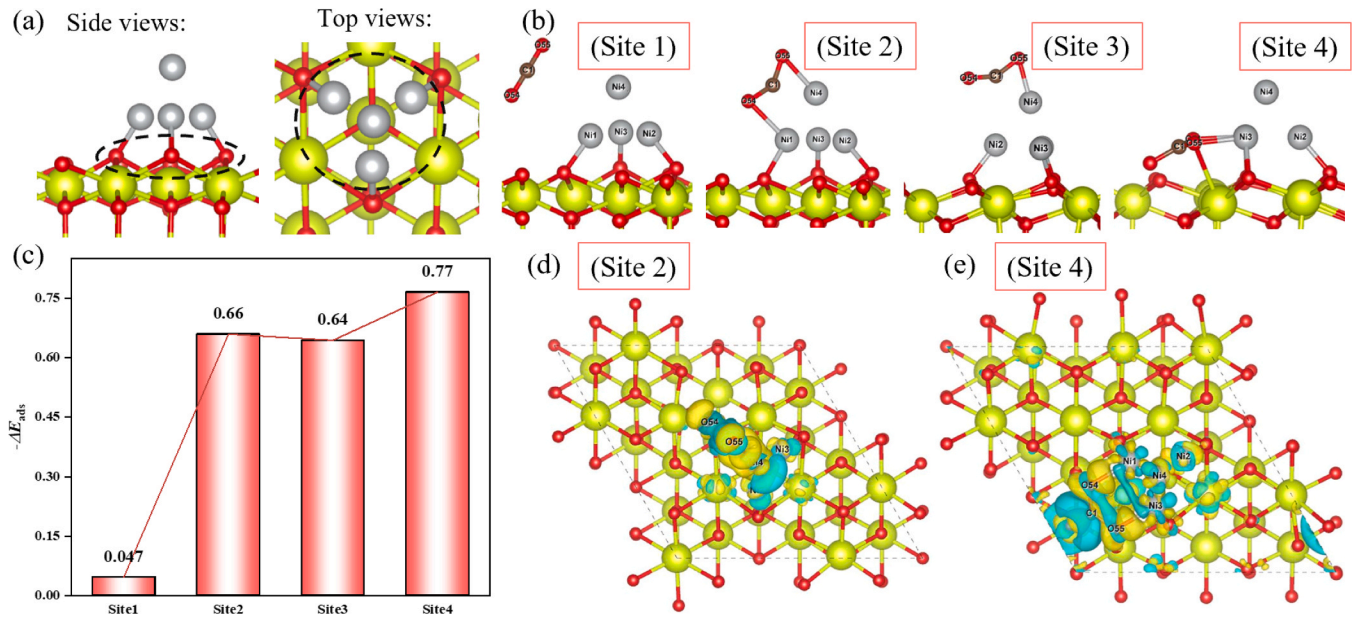

Fig. 11. (a) Ni_4/CeO_2 (111)-Perfect/Defect-Optimized configurations side and top view; (b), (c) The four different adsorption configuration and their ΔE_{ads} of CO_2 on defective Ni_4/CeO_2 (111) surface; (d), (e) Charge density difference distribution of CO_2 adsorption on defect configuration at site 2 and site 4: yellow (electron-rich)/ blue (electron-deficient).

Table 5
The C═O bond lengths ($D_{C=O54,\ 55}$), the bond angle of $O{=}C{=}O$, and the charge transfer to the adsorbed CO_2 on CeO_2 (111) supported Ni_4 cluster at site 1, site 2, site 3, site 4 (corresponding to Fig. 11b and d).

Site	*D:* $_{C=O54}$ *(Å)*	*D:* $_{C=O55}$ *(Å)*	*Angle:* $_{O=C=O}$ *(°)*	*ΔQ(e)*
1	1.178	1.178	179.2	/
2	1.235	1.253	142.0	−0.59
3	1.202	1.257	147.4	/
4	2.095	2.058	122.1	−0.49

bent with the bond angle of 122.1°. The bent shape is an activating CO_2 adsorbed on catalyst surface, but it does not mean the carbonate structure [58]. To further uncover the intrinsic causes of adsorption energy variations, the relevant electronic structure information was obtained. Additionally, considering that the ΔE_{ads} of site 2 and site 3 were quite close with each other, only sites 2 and 4 were calculated. Differential charge density and Bader charge analysis (Fig. 11(d), (f) and Fig. S5(a), (b)) showed that charge density redistribution occurred between CO_2 and Ni_4 cluster due to electron transfer from Ni to O atoms. The adsorbed CO_2 molecule was negatively charged (-0.59 |e|, −0.49 |e|, respectively), which indicated that the CO_2 molecule had been activated.

Projected density of states ($PDOS^1$) of the whole system adsorbing CO_2 on the sites 2 and 4 were calculated, which contributes to comprehending the activation progress of gas molecules on the catalyst surface accurately. Sites 2 and 4 showed mutual changes in some regions. Fig. 12(a), (c) and Fig. S6(a), (c) revealed that the s orbital of CO_2 at two sites was of no obvious change. The band of adsorbed CO_2 at two sites moved to higher energy level compared with isolated CO_2. The electron states of Partial density of states ($PDOS^2$) of all CO_2 are all contributed by s and p orbital electrons at low and high energy positions, respectively. Besides, an apparent overlap between the p orbital of CO_2 and d orbital of Ni originating from the interaction between Ni and CO_2 under Fermi energy level, which led to the original double degenerate $1\pi_g$ orbital of CO_2 having an apparent energy level spilt (Fig. 12(d), (f) and Fig. S6(d), (f)). However, the overlap of p orbitals of CO_2 and d orbitals of Ni between site 2 and site 4 was differed, with overlapping at site 4 being more obvious. This indicates differences in the interaction between CO_2 and substrate, corresponding to weak and strong adsorption behaviors on the Ni_4/CeO_2 (111) surface, respectively. Near the Fermi energy level (Fig. 12(f)), a new DOS contribution emerged resulting from the interaction between $2\pi^*$ orbital of CO_2 and d orbital of Ni, with the β spin orbital showing better energy matching. As aforementioned, those analyses indicate that the defect Ni_4/CeO_2 (111) surface is conducive to the activation of CO_2 molecules.

4. Conclusions

In this work, a series of MOFs derived Ni/CeO_2-X with various morphologies had been successfully fabricated and 10 wt% Ni was loaded via impregnation method, as well as their efficiencies were tested in catalyzing CO_2 hydrogenation to CH_4. Moreover, by combining theoretical calculations, we explored the adsorption and activation of CO_2 in Ni_4/CeO_2 catalyst surface. The following conclusions can be drawn from this study:

(1) The Ni/CeO_2 catalysts with different CeO_2 morphologies exhibited differences in catalytic performance for CO_2 methanation. Comprehensive characterization results demonstrated that Ni/CeO_2-BTC exhibited superior physical and chemical properties, including oxygen vacancies, specific surface area, and as well as catalytic activity in CO_2 conversion under the same conditions.
(2) It was found that Ni/CeO_2-BTC with rod-like structures exhibited the best CO_2 conversion in all testing conditions, although its methane selectivity was not the highest among all the samples. The metallic Ni particles achieve good dispersion on the MOF-derived CeO_2 support due to the special pore structure of the MOFs. Additionally, the redox couple of Ce^{3+}/Ce^{4+} associated with oxygen vacancy was also crucial for improving catalytic activity towards CO_2 reduction.
(3) DFT calculation also demonstrated that oxygen vacancies as the Lewis basic site were conducive to the adsorption and activation of CO_2 on the Ni_4/CeO_2 (111). Compared with the other adsorption sites in paper, it preferred adsorbing at the interface of Ni-O-Ce. This enhanced adsorption was ascribed to a stronger interaction between Ni and the adsorbate, which facilitated charge transfer and promoted CO_2 activation.

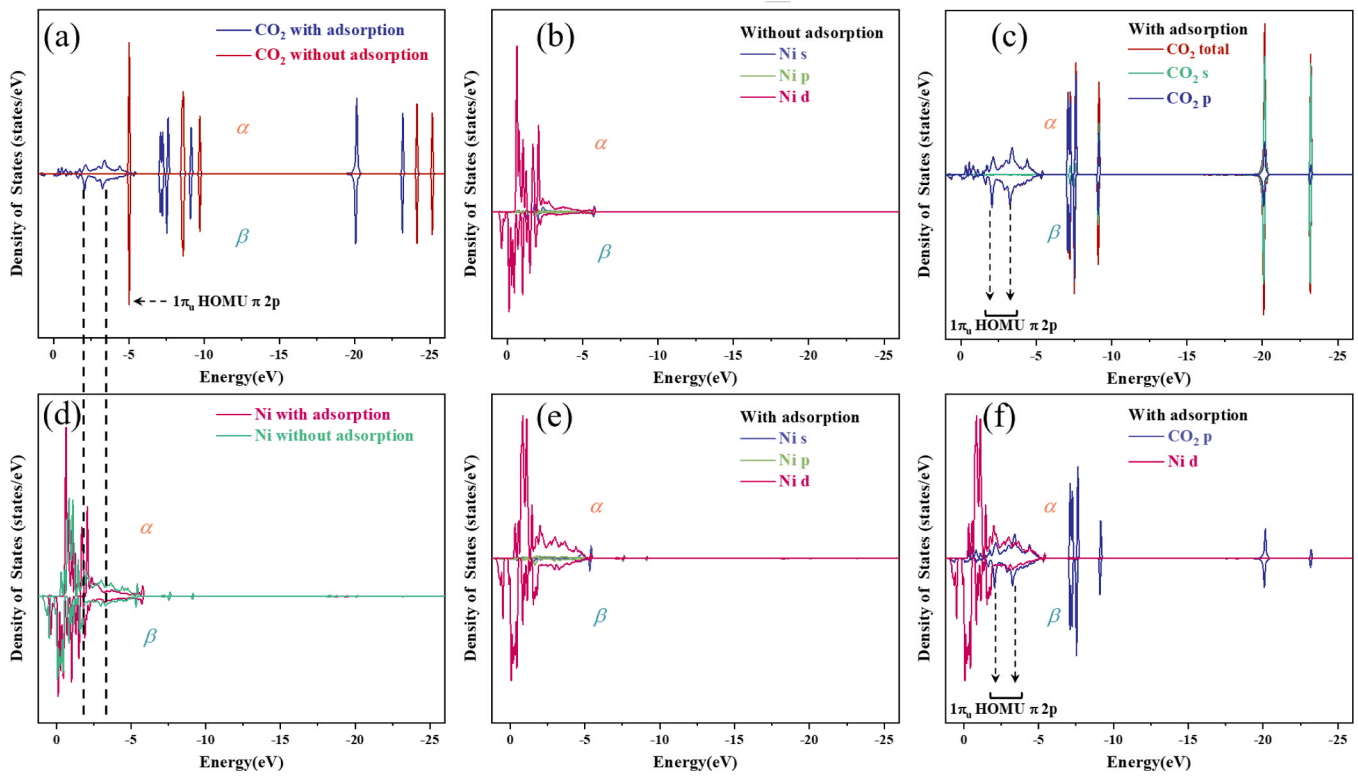

Fig. 12. (a), (d) Projected Density of States (PDOS[1]) of CO_2 and Ni of site 4 on defect configuration with and without adsorption; (b) Partial density of states (PDOS[2]) of Ni_4/CeO_2 (111) without adsorption; (c) PDOS[2] of s and p orbital of adsorbed CO_2 at site 4; (e) PDOS[2] of Ni s, p, d orbital interacting with O of CO_2 at site 4; (f) PDOS[2] of CO_2 p, Ni d orbital post-adsorption of site 4.

The significance of this study lies in exploring the performance of catalysts with various MOF morphologies in CO_2 reduction, potentially benefiting the synthesis of valuable chemical in the carbon circular economy. Given the complexity of the CO_2 methanation mechanism, advanced in-situ characterization methods are expected to be employed to thoroughly analyze the chemical state changes of intermediates and gradually clarify the reaction mechanism. In DFT simulation, factors such as multiple oxygen vacancies on the surface or bulk, the molecular dynamic and metal Ni loading are worth considering for a comprehensive investigation of reaction mechanisms from the atomic level. It is essential to broaden the application scope (Electrochemical catalysis, Green H_2 production and large-scale synthetic natural gas) in view of the superior physical and chemical properties of MOFs-derived catalyst in the future.

CRediT authorship contribution statement

Zehua Huang: Visualization, Supervision. **Xi Chen:** Formal analysis. **Jidong Lu:** Writing – review & editing, Project administration, Conceptualization. **Jinke Wu:** Writing – original draft, Software, Formal analysis, Data curation. **Meirong Dong:** Writing – review & editing, Visualization, Project administration, Funding acquisition. **Hongchuan Liu:** Writing – review & editing, Conceptualization. **Junshu Yang:** Data curation, Conceptualization.

Declaration of Competing Interest

The authors declare no competing financial interests or personal relationships that could have influenced this work.

Acknowledgement

The research was supported by the National Natural Science Foundation of China (No. 52376107) and Foundation of Science and Technology Projects in Guangzhou (2025A04J7048). We also acknowledge the support from the Fundamental Research Funds for the Central Universities (2022ZFJH04)

Appendix A. Supporting information

Supplementary data associated with this article can be found in the online version at doi:10.1016/j.jece.2025.118575.

Data availability

Data will be made available on request.

References

[1] A.D.N. Kamkeng, M. Wang, J. Hu, W. Du, F. Qian, Transformation technologies for CO_2 utilization: current status, challenges and future prospects, Chem. Eng. J. 409 (2021) 128–138.
[2] W.K. Fan, M. Tahir, Recent trends in developments of active metals and heterogenous materials for catalytic CO_2 hydrogenation to renewable methane: a review, J. Environ. Chem. Eng. 9 (2021) 35.
[3] Y.A. Alli, A. Bamisaye, M.O. Bamidele, N.O. Etafo, S. Chkirida, A. Lawal, V. O. Hammed, A.S. Akinfenwa, E. Hanson, C. Nwakile, Transforming waste to wealth: harnessing carbon dioxide for sustainable solutions, Results Surf. Interfaces 17 (2024) 100321.
[4] X. Su, P. Liu, Y. Mei, J. Qiu, The impact of carbon capture, utilization, and storage (CCUS) projects on environmental protection, economic development, and social equity, J. Clean. Prod. 482 (2024) 144218.
[5] C. Vogt, M. Monai, G.J. Kramer, B.M. Weckhuysen, The renaissance of the sabatier reaction and its applications on earth and in space, Nat. Catal. 2 (2019) 188–197.
[6] J. Chi, H. Yu, Water electrolysis based on renewable energy for hydrogen production, Chin. J. Catal. 39 (2018) 390–394.
[7] X. Su, J. Xu, B. Liang, H. Duan, B. Hou, Y. Huang, Catalytic carbon dioxide hydrogenation to methane: a review of recent studies, J. Energy Chem. 25 (2016) 553–565.
[8] C. Shen, M. Liu, S. He, H. Zhao, C. Liu, Advances in the studies of the supported ruthenium catalysts for CO_2 methanation, Chin. J. Catal. 63 (2024) 1–15.

[9] F. Zhang, W. Chen, W. Li, Recent advances in the catalytic conversion of CO_2 to chemicals and demonstration projects in China, Mol. Catal. 541 (2023) 113093.
[10] N. Schreiter, J. Kirchner, S. Kureti, A DRIFTS and TPD study on the methanation of CO_2 on Ni/Al_2O_3 catalyst, Catal. Commun. 140 (2020) 105988.
[11] K. Wang, Y. Men, S. Liu, J. Wang, Y. Li, Y. Tang, Z. Li, W. An, X. Pan, L. Li, Decoupling the size and support/metal loadings effect of Ni/SiO_2 catalysts for CO_2 methanation, Fuel 304 (2021) 121388.
[12] X. Jia, X. Zhang, N. Rui, X. Hu, C. Liu, Structural effect of Ni/ZrO_2 catalyst on CO_2 methanation with enhanced activity, Appl. Catal. BEnviron. 244 (2019) 159–169.
[13] X. Liu, C. Bao, Z. Zhu, H. Zheng, C. Song, Q. Xu, Thermo-photo synergic effect on methanol steam reforming over mesoporous Cu/TiO_2-CeO_2 catalysts, Int. J. Hydrog. Energy 46 (2021) 26741–26756.
[14] C. Paun, O.V. Safonova, J. Szlachetko, P.M. Abdala, M. Nachtegaal, J. Sa, E. Kleymenov, A. Cervellino, F. Krumeich, J.A. Van Bokhoven, Polyhedral CeO_2 nanoparticles: size-dependent geometrical and electronic structure, J. Phys. Chem. C. 116 (2012) 7312–7317.
[15] G. Zhou, H. Liu, K. Cui, A. Jia, G. Hu, Z. Jiao, Y. Liu, X. Zhang, Role of surface ni and ce species of Ni/CeO_2 catalyst in CO_2 methanation, Appl. Surf. Sci. 383 (2016) 248–252.
[16] J. Ashok, S. Pati, P. Hongmanorom, Z. Tianxi, C. Junmei, S. Kawi, A review of recent catalyst advances in CO_2 methanation processes, Catal. Today 356 (2020) 471–489.
[17] T.T.M. Nguyen, L. Wissing, M.S. Skj, Th-Rasmussen, high temperature methanation: catalyst considerations, Catal. Today 215 (2013) 233–238.
[18] A. Tsiotsias, N.D. Charisiou, E. Harkou, S. Hafeez, G. Manos, A. Constantinou, A.G. S. Hussien, A.A. Dabbawala, V. Sebastian, S.J. Hinder, M.A. Baker, K. Polychronopoulou, M.A. Goula, Enhancing CO_2 methanation over ni catalysts supported on sol-gel derived Pr_2O_3-CeO_2: an experimental and theoretical investigation, Appl. Catal. BEnviron. 318 (2022) 16.
[19] P. Hongmanorom, J. Ashok, P. Chirawatkul, S. Kawi, Interfacial synergistic catalysis over ni nanoparticles encapsulated in mesoporous ceria for CO_2 methanation, Appl. Catal. BEnviron. 297 (2021) 13.
[20] X. Tang, Z. Fang, Y. Wu, Z. Yuan, B. Deng, Z. Du, C. Sun, F. Zhou, X. Qiao, X. Li, Efficiency NiCu/t-zirconia catalysts for methanol steam reforming: experimental and DFT insights, Energy 297 (2024) 131293.
[21] R.R. Ikreedeegh, M. Tahir, A critical review in recent developments of metal-organic-frameworks (MOFs) with band engineering alteration for photocatalytic CO_2 reduction to solar fuels, J. CO_2 Util. 43 (2021) 101381.
[22] A.H. Anwer, M. Shoeb, F. Mashkoor, A. Ali, S. Kareem, M.Z. Ansari, J.M. Park, C. Jeong, Simultaneous reduction of carbon dioxide and energy harvesting using RGO-based SiO_2-TiO_2 nanocomposite for supercapacitor and microbial electrosynthesis, Appl. Catal. BEnviron. 339 (2023) 18.
[23] M.N. Khan, M. Shoeb, F. Mashkoor, K. Kim, M. Kang, J. Yu, H.S. Bae, I. Jang, C. Jeong, Exploring the integration of CNT interwoven VY-MOF nanostructured for enhanced electrochemical performance supercapacitor device and their charge storage mechanism, J. Energy Storage 127 (2025) 15.
[24] F. Mashkoor, M. Shoeb, J. Yoon, C. Jeong, Selective electrochemical detection of perfluorooctanoic acid (PFOA) using CNT-anchored SnO_2-WO_3 nanocomposites based sensor for real time analysis, J. Environ. Chem. Eng. 13 (2025) 10.
[25] F. Wang, J. Tian, M. Li, W. Li, L. Chen, X. Liu, J. Li, A. Muhetaer, Q. Li, Y. Wang, L. Gu, D. Ma, D. Xu, A photoactivated Cu-CeO_2 catalyst with Cu-[O]-Ce active species designed through MOF crystal engineering, Angew. Chem. Int. Ed. 59 (2020) 8203–8209.
[26] W. Cai, X. Yu, Y. Cao, C. Hu, Y. Wang, Y. Zhao, Y. Bu, Electron-coupled enhanced interfacial interaction of Ce-MOF/Bi_2MoO_6 heterostructure for boosted photoreduction CO_2, J. Environ. Chem. Eng. 10 (2022) 107461.
[27] X. Feng, K. Wang, M. Zhou, F. Li, J. Liu, M. Zhao, L. Zhao, X. Song, P. Zhang, L. Gao, Metal organic framework derived Ni/CeO_2 catalyst with highly dispersed ultra-fine ni nanoparticles: impregnation synthesis and the application in CO_2 methanation, Ceram. Int. 47 (2021) 12366–12374.
[28] H. Liu, M. Dong, J. Xiong, Z. Huang, H. Hou, Y. Liang, J. Lu, Study on Ce-MOF-derived oxides as morphology-tunable catalyst supports for dry reforming of methane, Appl. Surf. Sci. 679 (2025) 161167.
[29] J. Zhang, Y. Yang, J. Liu, B. Xiong, Mechanistic understanding of CO_2 hydrogenation to methane over Ni/CeO_2 catalyst, Appl. Surf. Sci. 558 (2021) 149866.
[30] Y. Guo, H. Zhu, H. Zhao, Q. Zhao, C. Zhou, B. Suo, W. Zou, Z. Jiang, Y. Li, A theoretical study of the electrochemical reduction of CO_2 on cerium dioxide supported palladium single atoms and nanoparticles, Phys. Chem. Chem. Phys. 23 (2021) 26185–26194.
[31] W. Sun, X. Li, C. Sun, Z. Huang, H. Xu, W. Shen, Insights into the pyrolysis processes of Ce-MOFs for preparing highly active catalysts of toluene combustion, Catalysts 9 (2019) 682.
[32] X. Chen, X. Chen, E. Yu, S. Cai, H. Jia, J. Chen, P. Liang, In situ pyrolysis of Ce-MOF to prepare CeO_2 catalyst with obviously improved catalytic performance for toluene combustion, Chem. Eng. J. 344 (2018) 469–479.
[33] M. Lammert, C. Glissmann, H. Reinsch, N. Stock, Synthesis and characterization of new Ce(IV)-MOFs exhibiting various framework topologies, Cryst. Growth Des. 17 (2017) 1125–1131.
[34] J. Hafner, Ab-initio simulations of materials using VASP: Density-functional theory and beyond, J. Comput. Chem. 29 (2008) 2044–2078.
[35] V. Wang, N. Xu, J. Liu, G. Tang, W. Geng, VASPKIT: a user-friendly interface facilitating high-throughput computing and analysis using VASP code, Comput. Phys. Commun. 267 (2021) 2044–2078.
[36] G. Kresse, D. Joubert, From ultrasoft pseudopotentials to the projector augmented-wave method, Phys. Rev. B 59 (1999) 1758–1775.
[37] J.P. Perdew, K. Burke, M. Ernzerhof, Generalized gradient approximation made simple, Phys. Rev. Lett. 78 (1997) 1396.
[38] N. Baumann, J. Lan, M. Iannuzzi, CO_2 adsorption on the pristine and reduced CeO_2 (111) surface: geometries and vibrational spectra by first principles simulations, J. Chem. Phys. 154 (2021) 094702.
[39] J. Ren, C. Mebrahtu, R. Palkovits, Ni-based catalysts supported on Mg-Al hydrotalcites with different morphologies for CO_2 methanation: exploring the effect of metal-support interaction, Catal. Sci. Technol. 10 (2020) 1902–1913.
[40] Y. Liu, D. Li, H. Zhao, C. Wang, Y. Xu, L. Li, Z. Li, H. Wang, K. Li, Boosting CO_2 methanation activity by tuning ni crystal plane and oxygen vacancy in Ni/CeO_2 catalyst, Chem. Eng. J. 494 (2024) 153004.
[41] R. Ye, Q. Li, W. Gong, T. Wang, J.J. Razink, L. Lin, Y. Qin, Z. Zhou, H. Adidharma, J. Tang, A.G. Russell, M. Fan, Y. Yao, High-performance of nanostructured Ni/CeO_2 catalyst on CO_2 methanation, Appl. Catal. BEnviron. 268 (2020) 118474.
[42] R. Tang, N. Ullah, Y. Hui, X. Li, Z. Li, Enhanced CO_2 methanation activity over Ni/CeO_2 catalyst by one-pot method, Mol. Catal. 508 (2021) 118474.
[43] S. Ratchahat, M. Sudoh, Y. Suzuki, W. Kawasaki, R. Watanabe, C. Fukuhara, Development of a powerful CO_2 methanation process using a structured Ni/CeO_2 catalyst, J. CO_2 Util. 24 (2018) 210–219.
[44] K. Liu, H. You, G. Jia, Y. Zheng, Y. Huang, Y. Song, M. Yang, L. Zhang, H. Zhang, Hierarchically nanostructured coordination polymer: facile and rapid fabrication and tunable morphologies, Cryst. Growth Des. 10 (2010) 790–797.
[45] S. Liu, S. Niu, H. Yu, K. Han, S. Xia, Z. Yang, Y. Zheng, Y. Zhang, Y. Hao, A. Abulizi, Electrolysis combined with magnetic CeO_2/ZSM-5@Fe_3O_4 catalyst to boost transesterification for biodiesel production, Fuel 378 (2024) 132862.
[46] H. Yu, J. Sun, X. Chen, B. Wang, X. Liang, M. Gao, H. Si, Synthesis of a novel acid-base bifunctional Zn/Ca-Zr catalyst for biodiesel application: experimental and molecular simulation studies, Renew. Energy 217 (2023) 191138.
[47] S.W.K. Sing, Reporting physisorption data for gas/solid systems with special reference to the determination of surface area and porosity (recommendations 1984), Pure Appl. Chem. 57 (1985) 603–619.
[48] A. Westermann, B. Azambre, M.C. Bacariza, I. Graca, M.F. Ribeiro, J.M. Lopes, C. Henriques, Insight into CO_2 methanation mechanism over NiUSY zeolites: an operando IR study, Appl. Catal. BEnviron. 174 (2015) 120–125.
[49] B. Ouyang, W. Tan, B. Liu, Morphology effect of nanostructure ceria on the Cu/CeO_2 catalysts for synthesis of methanol from CO_2 hydrogenation, Catal. Commun. 95 (2017) 36–39.
[50] A. Kazemi, M.A. Pordsari, M. Tamtaji, M.H. Afshari, S. Keshavarz, F. Zeinali, H. Baesmat, S. Zahiri, F. Manteghi, A. Ghaemi, S. Rohani, W.A. Goddard, Unveiling the power of defect engineering in MOF-808 to enhance efficient carbon dioxide adsorption and separation by harnessing the potential of DFT analysis, Chem. Eng. J. 494 (2024).
[51] X. Zuo, S. Ma, Q. Wu, J. Xiong, J. He, C. Ma, Z. Chen, Nanometer CeO_2 doped high silica ZSM-5 heterogeneous catalytic ozonation of sulfamethoxazole in water, J. Hazard. Mater. 411 (2021).
[52] K.M. Eblagon, P.H. Concepcion, H. Silva, A. Mendes, Ultraselective low temperature steam reforming of methanol over PdZn/ZnO catalysts influence of induced support defects on catalytic performance, Appl. Catal. BEnviron. 154 (2014) 316–328.
[53] F. Jiang, S. Wang, B. Liu, J. Liu, L. Wang, Y. Xiao, Y. Xu, X. Liu, Insights into the influence of CeO_2 crystal facet on CO_2 hydrogenation to methanol over Pd/CeO_2 catalysts, ACS Catal. 10 (2020) 11493–11509.
[54] S. Lin, L. Kang, L. Gong, L. Tao, S. Xi, Z. Li, W. Liu, Facet specificity of yttrium doping on CO_2 methanation over Ni/CeO_2 catalysts, Chem. Eng. J. 502 (2024) 13.
[55] C. Italiano, J. Llorca, L. Pino, M. Ferraro, V. Antonucci, A. Vita, CO and CO_2 methanation over ni catalysts supported on CeO_2, Al_2O_3 and Y_2O_3 oxides, Appl. Catal. BEnviron. 264 (2020) 16.
[56] S. Lin, Z. Li, M. Li, Tailoring metal-support interactions via tuning CeO_2 particle size for enhancing CO_2 methanation activity over Ni/CeO_2 catalysts, Fuel 333 (2023) 14.
[57] W. Yang, K. Chang, M. Yang, X. Yan, S. Yang, Y. Liu, G. Wang, F. Xia, H. Wang, Q. Zhang, Facilitating CO_2 methanation over oxygen vacancy-rich Ni/CeO_2: insights into the synergistic effect between oxygen vacancy and metal-support interaction, Chem. Eng. J. 499 (2024) 156493.
[58] N. Kumari, M.A. Haider, M. Agarwal, N. Sinha, S. Basu, Role of reduced CeO_2 (110) surface for CO_2 reduction to CO and methanol, J. Phys. Chem. C. 120 (2016) 16626–16635.